NANO · MICRO small
www.small-journal.com

Boosting the Performance of Graphene Cathodes in Na–O_2 Batteries by Exploiting the Multifunctional Character of Small Biomolecules

Marina Enterría, Juan Luis Gómez-Urbano, Jose María Munuera, Silvia Villar-Rodil, Daniel Carriazo, Juan Ignacio Paredes,* and Nagore Ortiz-Vitoriano**

Graphene aerogels derived from a biomolecule-assisted aqueous electrochemical exfoliation route are explored as cathode materials in sodium–oxygen (Na–O_2) batteries. To this end, the natural nucleotide adenosine monophosphate (AMP) is used in the multiple roles of exfoliating electrolyte, aqueous dispersant, and functionalizing agent to access high quality, electrocatalytically active graphene nanosheets in colloidal suspension (bioinks). The surface phenomena occurring on the electrochemically derived graphene cathode is thoroughly studied to understand and optimize its electrochemical performance, where a cooperative effect between the nitrogen atoms and phosphates from the AMP molecules is demonstrated. Moreover, the role of the nitrogen atoms in the adenine nucleobase of AMP and short-chain phosphate is unraveled. Significantly, the use of such cathodes with a proper amount of AMP molecules adsorbed on the graphene nanosheets delivers a discharge capacity as high as 9.6 mAh cm^{-2} and performs almost 100 cycles with a considerably reduced cell overpotential and a coulombic efficiency of ≈97% at high current density (0.2 mA cm^{-2}). This study opens a path toward the development of environmentally friendly air cathodes by the use of natural nucleotides which offers a great opportunity to explore and manufacture bioinspired cathodes for metal–oxygen batteries.

1. Introduction

Rechargeable batteries constitute the nexus between renewable energy sources and stationary and mobile applications, such as the electric vehicle and electronic portable devices. Indeed, the development of batteries with improved features (e.g., higher energy density, longer cycle life, safer deployment, and lower weight)—produced by cheaper and more environmentally friendly procedures with nontoxic components—is poised to play a crucial role in the transition to a fossil fuel-free economy.[1] However, lithium-ion batteries (LiBs), which currently dominate the battery market, suffer from low energy density for some of the above-mentioned applications. In addition, the overall scarcity of lithium sources and their limited distribution to some specific areas of the Earth's crust can result in serious sociopolitical conflicts in the future.[2] For these reasons, "beyond lithium ion" energy storage systems are urgently needed. Among the different emerging battery systems, sodium–oxygen (Na–O_2) batteries have shown to be very promising due to their high theoretical energy density, which is ≈5–10 times higher than that of LiBs (100–265 vs 1108 Wh kg^{-1}). Na–O_2 batteries involve the electrochemical reduction of molecular oxygen [oxygen reduction reaction (ORR)] at the "air-cathode" and further formation/accommodation of sodium oxides on the cathode surface during discharge. The nucleation and growth of different discharge products (i.e., different sodium oxides) can take place either in the electrolyte bulk to further precipitate on the cathode (solution-mediated mechanism) or directly at the cathode surface (surface-mediated

M. Enterría, J. L. Gómez-Urbano, D. Carriazo, N. Ortiz-Vitoriano
Centre for Cooperative Research on Alternative Energies (CIC energiGUNE)
Basque Research and Technology Alliance (BRTA)
Alava Technology Park
Albert Einstein, 48, Vitoria-Gasteiz 01510, Spain
E-mail: menterria@cicenergigune.com; nortiz@cicenergigune.com

The ORCID identification number(s) for the author(s) of this article can be found under https://doi.org/10.1002/smll.202005034.

DOI: 10.1002/smll.202005034

J. L. Gómez-Urbano
Departamento de Química Inorgánica
Universidad del País Vasco UPV/EHU
P.O. Box 664, Bilbao 48080, Spain

J. M. Munuera, S. Villar-Rodil, J. I. Paredes
Instituto de Ciencia y Tecnología del Carbono
INCAR-CSIC
C/Francisco Pintado Fe 26, Oviedo 33011, Spain
E-mail: paredes@incar.csic.es

D. Carriazo, N. Ortiz-Vitoriano
IKERBASQUE
Basque Foundation for Science
Bilbao 48013, Spain

mechanism).[3] During charge, the as-formed discharge products are decomposed back into molecular oxygen by an oxygen evolution reaction (OER) process.[4] The chemistry of the discharge products and their growth mechanisms are critically related to the energy density and the rechargeability of the battery and, consequently, a deep understanding of their formation/redissolution is required for achieving high-performance metal–air devices.[5] The prevalence of a given growth mechanism over any other is determined by the nature of the constituent elements of the electrochemical cell, such as the electrolyte or the presence of catalytically active functional groups on the cathode surface. Regarding the latter, it is known that certain functional groups on the cathode surface can catalyze the ORR by acting as nucleation sites[6–8] for the growth of the discharge products while facilitating their oxidation and redissolution during OER.[8,9] Despite their high energy density, Na–O_2 batteries are still in an early stage of development, with several challenges to overcome regarding reversible cycling (e.g., Na dendrite growth, side reactions, stability of the electrolyte, poor kinetics, etc.) for prospective commercialization. In this regard, the development of a suitable cathode material can help to address many of these issues by enhancing the kinetics of both ORR and OER; thus, accommodating larger amounts of discharge products and minimizing pore clogging.[10] Carbon materials have been largely used as electrodes in metal–O_2 (M = Na, Li) batteries due to their low cost, high surface area, chemical stability, high conductivity, developed porosity, and intrinsic catalytic activity toward the ORR/OER.[11,12] Among the different carbon-based cathode materials reported in the literature (carbon nanotubes,[13] carbon-metal,[14] and carbon-metal-oxide composites,[15–17] heteroatom-doped carbon or graphene,[18–20] bifunctional carbon materials combining metals and heteroatoms,[21] hierarchical porous carbon spheres,[22] or porous graphene[23]), graphene is a very promising candidate due to its 2D structure and electrical conductivity. In addition, properly constructed graphene-based materials can provide suitable channels for O_2 diffusion, facilitate impregnation by the electrolyte and offer a large number of active sites for the formation and decomposition of the discharge products.[24] However, the large-scale production of high-quality graphene as well as its processability are still challenging, as the sheets tend to easily restack by van der Waals or capillary forces, which compromises their high surface area and the accessibility of ions and molecules into and within the cathode. In this regard, the 3D assembly of the graphene nanosheets can avoid restacking and thus translate the properties of 2D graphene into macroscopic 3D porous materials.[25] In many cases, the development of such architectures requires the preparation and processing of colloidally stable graphene suspensions (inks), particularly in water for safety and sustainability reasons. To this end, the chemical exfoliation of graphite (i.e., the graphite oxide route) has arisen as the most popular strategy to produce highly dispersible graphene inks for the preparation of electrodes for electrochemical energy storage.[26] However, this time-consuming method implies the use of hazardous reactants (strong acids and oxidants) and multiple steps to obtain graphite oxide, followed by tedious washing and a postsynthesis step to yield an electrically conductive form of graphene, namely, reduced graphene oxide (rGO).[27] By contrast, the electrochemical exfoliation of graphite, particularly under anodic conditions, is a much simpler and faster method that has emerged in recent years as a promising alternative (new-generation graphene) to the graphite oxide route, especially with a view to energy-related applications.[28] The anodic exfoliation route involves the application of positive potentials to graphite in order to intercalate anions within its structure, leading to its structural expansion and delamination into graphene flakes. Furthermore, the exfoliation can be conducted under environmentally friendly conditions, notably in aqueous electrolytes that make use of innocuous biomolecules as the intercalating anion. More specifically, we have very recently introduced natural nucleotides as exfoliating agents for the electrochemical delamination of graphite, providing high quality and water-dispersible graphene nanosheets in a single-step process.[7] These nucleotides adsorb onto the graphene surface by noncovalent, π–π stacking of their nucleobase, while their sugar-phosphate moiety is oriented outward from the surface to produce a hydrophilic outer shell. This natural surfactant effect facilitates the colloidal stabilization of the graphene nanosheets in aqueous medium and its further processing into 3D assemblies.[29] In our previous work,[7] the use of graphene suspensions stabilized by the nucleotide adenosine monophosphate (AMP) enabled the preparation of porous graphene aerogels which presented a promising performance as NaO_2 battery cathodes by delivering 50 charge/discharge cycles at 0.2 mA cm^{-2} to 0.5 mAh cm^{-2} in a glyme-based electrolyte. The performance of the cathode was not further optimized while the role of the adsorbed AMP molecules during battery operation was left unexplored.

Herein, an in-depth analysis of this novel graphene-based material is conducted in order to understand the multiple roles of the AMP nucleotide in the processes occurring at the cathode. Moreover, optimization of cathode material allowed us to reach almost 100 cycles and 9.65 mAh cm^{-2} of capacity during discharge at the relatively high current density of 0.2 mA cm^{-2}. The performance of this novel graphene cathode was compared with that of reduced graphene oxide aerogels and other state-of-the art carbon-based Na–O_2 battery cathodes, where the areal capacity and cyclability values clearly outperformed those of such existing reference materials.

2. Experimental Section

Preparation of Graphene Suspensions and Graphene Aerogels: The electrochemically exfoliated graphene (EEG) nanosheets were prepared following a previously reported method.[7] Briefly, a graphite foil (25 × 35 × 0.5 mm^3, from Mersen) was anodically exfoliated using a platinum foil (25 × 25 × 0.025 mm^3) as cathode and 0.1 M aqueous solution of adenosine 5′-monophosphate disodium salt (AMP, obtained from Sigma Aldrich, ≥ 99.0% HPLC) as electrolyte. The two electrodes were placed at a distance of ≈2 cm, immersed in the electrolytic medium and connected to an Agilent 6614C DC power supply to apply a positive potential of 10 V to the graphite foil for 1 h, which led to its expansion and delamination. The as-expanded graphite foil was then bath-sonicated (J.P. Selecta Ultrasons system; frequency: 40 kHz; power: 22 W L^{-1}) for 3 h in the same electrolytic

solution to extract individually dispersed graphene nanosheets. The resulting suspension was subjected to two cycles of high-speed centrifugation (15 000 × *g*, 20 min) to completely sediment the material, followed by redispersion of the sediment in deionized water by 10 min of sonication. After this washing step, the dispersion was subjected to low-speed centrifugation (200 × *g*, 20 min) to separate poorly delaminated components (sediment) from the well exfoliated nanosheets retained in the supernatant (referred to as the EEG suspension). A second graphene dispersion (denoted as EEG-C suspension) was prepared by applying four additional washing cycles of sedimentation (15 000 × *g*, 20 min) and redispersion in pure water to the EEG suspension (EEG-C suspension). For comparative purposes, a commercial aqueous GO dispersion (obtained from Graphenea; concentration: 4 mg mL^{-1}, denoted as GO suspension) was also used to prepare rGO aerogel cathodes. The concentration of all the graphene-based dispersions (GO, EEG, and EEG-C) was determined by UV–vis absorption spectroscopy (Helios α spectrophotometer, Thermo Spectronics) through the Lambert-Beer's law. The absorbance was measured at a wavelength of 231 nm (GO) and 660 nm (EEG and EEG-C), using extinction coefficients of ε_{231} = 4008 mL mg^{-1} m^{-1} for GO[30] and ε_{660} = 2440 mL mg^{-1} m^{-1} for EEG and A-EEG-C.[31] The concentration of all the dispersions was further adjusted to 2 mg mL^{-1} prior to the preparation of the graphene-based aerogels. A volume of 40 mL of each dispersion was frozen by immersion in liquid N_2 (–176 °C) and subsequently freeze-dried (Telstar LyoQuest equipment) for 72 h. The as-obtained monolithic aerogels (Figure S1a,b, Supporting Information) were compacted (Figure S1c, Supporting Information) and punched out to obtain disc-shaped electrodes of 11cm in diameter and 0.95 cm^2 in area (Figure S1d,e, Supporting Information). The GO-derived discs were heated at 5 °C min^{-1} under 80 mL min^{-1} argon flow up to 800 °C, and this temperature was kept for 1 h to obtain the rGO aerogel cathodes (A-rGO, 1.5 ± 0.3 mg). The discs were cooled down to room temperature under the same argon flow. Aerogel discs prepared from the EEG graphene dispersion were either not subjected to thermal treatment (A-EEG, 4.1 ± 0.4 mg) or pyrolyzed at different temperatures, namely, 400 °C (A-EEG-400, 3 ± 0.3 mg) and 800 °C (A-EEG-800, 2.1 ± 0.3 mg) using the conditions described above. Another batch of aerogels with reduced AMP content was prepared by freeze-drying the EEG-C dispersion (A-EEG-C, 3 ± 0.5 mg). Prior to be used as cathodes, all the graphene aerogel discs were dried at 200 °C under vacuum for 12 h and transferred to the glove box without exposure to air. All the materials used in this study are summarized in **Table 1**.

Table 1. Summary of the materials along with the acronyms used in this work.

Sample	Description	Treatment applied
GO	Commercial graphene oxide suspension	As-received
EEG	Anodic exfoliated graphene suspension	2 washing cycles of sedimentation and redispersion in water
EEG-C	Anodic exfoliated graphene suspension	6 washing cycles of sedimentation and redispersion in water
A-rGO	Reduced graphene oxide aerogel	Freeze drying GO suspension/800 °C under argon
A-EEG	Anodic exfoliated graphene aerogel	Freeze drying EEG suspension
A-EEG-C	Anodic exfoliated graphene aerogel	Freeze drying EEG-C suspension
A-EEG-200	Anodic exfoliated graphene aerogel	A-EEG aerogel heated at 200 °C for 12 h under vacuum
A-EEG-400	Anodic exfoliated graphene aerogel	A-EEG aerogel pyrolyzed at 400 °C for 12 h under argon
A-EEG-800	Anodic exfoliated graphene aerogel	A-EEG aerogel pyrolyzed at 800 °C for 12 h under argon

Physicochemical Characterization: The porous texture of the electrodes was examined by N_2 adsorption–desorption analysis at –196 °C using an ASAP 2020 adsorption analyzer (Micromeritics), where samples were degassed under vacuum at 200 °C for 12 h. The morphological characterization of pristine and discharged electrodes was conducted by scanning electron microscopy (SEM) using a FEI Quanta 250 microscope operating at 20 kV. Atomic force microscopy (AFM) measurements were accomplished with a Nanoscope IIIa Multimode apparatus working in the tapping mode of operation with rectangular silicon cantilevers (nominal spring constant: 40 N m^{-1}; resonance frequency: 250–300 kHz). Specimens for AFM were prepared by drop-casting a small volume (20–40 µL) of graphene dispersion (≈0.1 mg mL^{-1}) onto a SiO_2 (300 nm)/Si substrate that was preheated at 50–60 °C and then allowed to dry. The thickness of the graphene nanosheets was estimated from AFM line profiles, subtracting a positive height offset of 0.5–1 nm that is generally introduced by SiO_2/Si supports.[32] Raman spectra of pristine aerogel cathodes were recorded with a Renishaw spectrometer (Nanonics Multiview 2000) operating with an excitation wavelength of 532 nm. The spectra were obtained by performing 5 acquisitions with 30 s of dwell time. Thermogravimetric analysis (TGA) was conducted on a TG209 F1 Libra equipment in argon atmosphere with a heating rate of 5 °C min^{-1} from 50 to 1000 °C. The materials were also analyzed by X-ray photoelectron spectroscopy (XPS), which was accomplished on a SPECS system working at a pressure around 10^{-7} Pa with a monochromatic Al K_α X-ray source (1486.7 eV) operated at 14.00 kV and 150 W. Samples were stuck on the XPS sample holder by means of double-sided carbon adhesive tape. Transmission electron microscopy (TEM) images of the aerogels were recorded in a JEOL 1011 microscope operated at an acceleration voltage of 80 kV. For the preparation of the specimens, the hydrogels were mixed with isopropanol at a nominal concentration of 0.5 mg mL^{-1} and bath-sonicated for 1 min. The resulting suspensions were drop-cast (≈20 µL) onto copper grids (200 mesh) covered with lacey carbon (acquired from Micro to Nano Supplies). The nature of the battery discharge products was studied by powder X-ray diffraction (XRD) using a Bruker D8 Discover diffractometer with $\theta/2\theta$ Bragg–Brentano geometry (monochromatic Cu radiation: $K_{\alpha 1}$ = 1.54056 Å) within the 30–60° range (2θ). Attenuated total reflection Fourier transform infrared (ATR-FTIR) spectrophotometry was performed on a Spectrum 400 DTGS PERKIN-ELMER. The analysis chamber was flushed with argon for 1 h prior to the sample analysis in order to avoid the decomposition of the discharge products when analyzing sensitive samples. Raman spectra for the discharged samples were recorded by focusing with a 50 × long working distance objective. The spectra were

obtained by performing 10 acquisitions with 10 s of exposure time of the laser beam to the sample. A silicon wafer was used for calibration. An in-house air-tight holder was used for the measurements. The pristine aerogel materials were not dried prior to TEM, TGA, SEM, and XPS analysis in order to evaluate their hygroscopic character. In order to analyze the effect of the drying step on the physicochemical properties of the materials, one of the A-EEG aerogel discs was dried under vacuum at the same conditions as the cathodes prior to the cell assembly (A-EEG-200). For the characterization of discharged electrodes, the cathodes were washed previously with fresh anhydrous 1,2 dimethoxyethane (DME, Sigma Aldrich) in an Ar-filled glove box to remove the excess of salt. The cleaned electrodes were subsequently transferred from the Ar-filled glove box to the SEM or XRD using an air-tight holder to avoid air exposure.

Cell Assembly and Electrochemical Characterization: A pressurized 2-electrode Swagelok-type cell was used for the galvanostatic measurements. The cells were dried overnight and transferred to an Ar-filled glove box (H_2O < 0.1 ppm, O_2 < 0.1 ppm, Jacomex, France). Regarding electrolyte preparation, DME solvent was used after drying over molecular sieves (3 Å, Sigma Aldrich) for one week. Sodium hexafluorophosphate ($NaPF_6$, 99% Stella Chemifa) and sodium perchlorate ($NaClO_4$, 98% Sigma-Aldrich) were employed as conductive salts after drying under vacuum at 120 °C for 24 h. 0.1 M $NaClO_4$ in DME and 0.1 M $NaPF_6$ in DME electrolytes were prepared after vigorously stirring proper mixtures of conductive salts and solvent. The electrolyte solutions prepared in the glove box presented water content values below 8 ppm (determined by C20 Karl Fisher coulometer, Mettler Toledo). Stainless steel mesh (1.13 cm^2, Alfa Aesar) was used as current collector for the air cathode, Celgard H2010 as separator and a sodium disc (0.95 cm^2) as reference and counter electrode. The assembled cells were pressurized with pure oxygen to ≈1 atm and a resting period of 8 h at open circuit voltage (≈2.2–2.3 V vs Na^+/Na) was set up. Galvanostatic deep-discharge and shallow cycling measurements were performed in a Biologic-SAS VMP3 potentiostat at a current density of 0.2 mA cm^{-2} in a potential range of 1.8–3.2 V versus Na^+/Na.

3. Results and Discussion

3.1. Graphene-Based Materials Characterization

The lateral size and thickness of the nanosheets in the GO and EEG suspensions were examined and compared by AFM. The EEG nanosheets tended to be smaller in lateral size (**Figure 1**a, ≈0.4–0.2 µm) than their GO counterparts (Figure 1b, ≈0.7–1.6 µm). Line profiles taken from the images revealed that the nanosheets in the EEG dispersion were generally thicker than those in the GO dispersion (typically single-layer for GO vs few-layers for EEG). Freeze-drying of both graphene-based suspensions (i.e., GO and EEG) led to free-standing, monolithic porous aerogels (Figure S1a,b, Supporting Information) which suggested the positive effect of the AMP nucleotide on the assembling of the EEG nanosheets (this point will be further discussed below).[33] The structural order of the nanosheets in aerogels prepared from the EEG and GO dispersions (i.e., A-EEG and A-rGO aerogels) was studied by Raman spectroscopy (Figure 1c). Both materials displayed the well-known D (1350 cm^{-1}) and G (1590 cm^{-1}) bands that are characteristic of graphite/graphene-based materials.[34] The D band, known as the defect band, is ascribed to the breathing vibration of sp^2-hibridized, aromatic carbon rings located next to an edge or defect in the lattice, while the G band arises from the stretching vibration of sp^2-based C—C bonds.

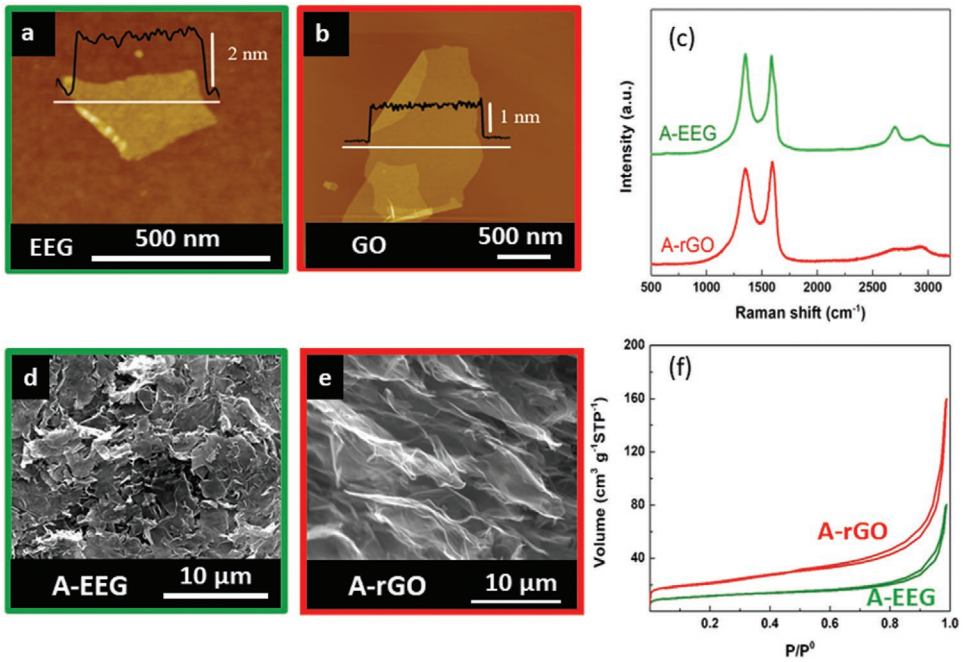

Figure 1. a) AFM images of GO and b) EEG nanosheets. c) Raman spectra, d,e) SEM images, and f) N_2 adsorption/desorption isotherms at –196 °C for aerogels prepared from GO (red trace) and EEG (green trace) suspensions (A-rGO and A-EEG, respectively).

The defect-related D band was measured to be wider for A-rGO than it was for A-EEG (full width at half maximum of 139 cm^{-1} for A-rGO vs 88 cm^{-1} for A-EEG), which indicates the presence of a larger number of defects in the former. The higher degree of order in A-EEG was also revealed by more defined and sharper bands in the second order Raman region of the spectra (2400–3300 cm^{-1}), and particularly by the emergence of a well-defined 2D band at about 2700 cm^{-1}.[32,34] It can thus be concluded that the EEG suspension consists of smaller, thicker and less defective graphene nanosheets than its GO counterpart. Accordingly, SEM images showed that the A-EEG aerogel was comprised of small and relatively aggregated sheets (Figure 1d). By contrast, a more open structure was observed for the A-rGO aerogel with large pores in-between large, wrinkled nanosheets (Figure 1e). This is in agreement with the TEM images (Figure S2, Supporting Information), where A-rGO aerogel appeared to be less densely aggregated than A-EEG and formed by the assembly of nanosheets of a few monolayers in thickness. The porous character of both A-EEG and A-rGO was confirmed by their N_2 adsorption–desorption isotherms, which correspond to meso-macroporous materials (Figure 1f). In agreement with the SEM images, the A-rGO aerogel exhibited larger mesopore volume, total pore volume and specific surface area than those of A-EEG (Table S1, Supporting Information).

3.2. Electrochemical Testing and Postmortem Characterization of Graphene Aerogel Cathodes

A-rGO and A-EEG cathodes were discharged to full capacity using two different electrolytes in order to study their electrochemical performance (**Figure 2**a). A-EEG cathode provided larger areal capacity values than A-rGO either for 0.1 M $NaClO_4$ in 1,2 dimethoxyethane (DME) (6.9 vs 5.7 mAh cm^{-2}) or 0.1 M $NaPF_6$ in DME (6.9 vs 4.9 mAh cm^{-2}) electrolytes. The use of $NaPF_6$ as conducting salt resulted in a decrease in the discharge overpotential [≈120 mV vs $E_0(NaO_2)$ = 2.27 V] for both cathodes relative to the use of $NaClO_4$, where A-EEG presented a stable voltage plateau at 2.10 V up to 3.5 mAh cm^{-2}. However, deeper discharge of A-EEG cathode resulted in a highly irregular discharge profile when using 0.1 M $NaPF_6$ in DME. The as-discharged electrodes were further characterized to identify the nature of the discharge products as well as their morphology. Sodium superoxide (NaO_2) was identified as the main discharge product by powder X-ray diffraction (XRD) for all the studied conditions (i.e., cathodes and electrolytes). Nevertheless, a little contribution of $Na_2O_2 \cdot 2H_2O$ was also observed in all the XRD patterns (Figure S3, Supporting Information).[35] The chemical stability of A-EEG and A-rGO cathodes against the strong oxidizing nature of ORR products (i.e., NaO_2 and $Na_2O_2 \cdot 2H_2O$) was studied. To that aim, the surface of the discharged cathodes was cleaned and analyzed by XPS. Comparison of the high-resolution C 1s and O 1s core level spectra of both cathodes before and after being discharged reveal that they are stable, hence, not substantial oxidization was verified during the discharge process (Figure S4, Supporting Information). Significant differences in the morphology and size of the discharge products were observed by SEM imaging as a function of both the cathode and the electrolyte. Specifically, NaO_2 cubes of 5–10 µm in size were identified on the surface of A-rGO cathodes in 0.1 M $NaClO_4$ in DME (Figure 2b), while slightly larger particles were observed with 0.1 M $NaPF_6$ in DME (Figure 2c). In contrast, A-EEG yielded significantly smaller cubes (≤4µm, Figure 2d) with 0.1 M $NaClO_4$ in DME and the discharge products for the cathode discharged in 0.1 M $NaPF_6$ in DME were even hard to discern (Figure 2e). The influence of the surface properties of the air electrode on the growth of the discharge products has been previously observed.[7–9] Hence, small-size particles or film-like deposition products similar to those observed in Figure 2e were associated to a surface-mediated mechanism. Nevertheless, the prevalence of this mechanism over the solution-mediated has been mainly correlated with the applied current density[36] or the use of additives[37] rather than the chemistry of the cathode. In our previous work, an increased interaction of reduce oxygen species with the phosphate groups of AMP molecules was suggested to promote a surface-mediated mechanism in A-EEG aerogels.[7]

The cycling performance of the graphene-based cathodes was evaluated by galvanostatic charge/discharge measurements at 0.2 mA cm^{-2} in shallow-cycling experiments, limiting the depth of discharge to 0.5 mAh cm^{-2} (**Figure 3**). Regardless of the electrolyte, the A-EEG cathodes yielded larger cell

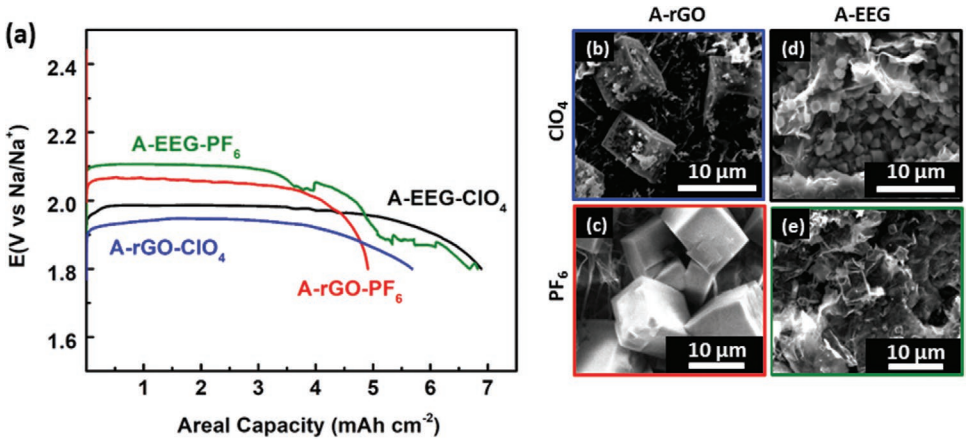

Figure 2. a) Galvanostatic deep-discharge curves of A-rGO and A-EEG cathodes at 0.2 mA cm^{-2} using 0.1 M $NaClO_4$ and $NaPF_6$ in DME electrolytes and b–e) SEM images framed with the same color code used for the respective discharged electrodes.

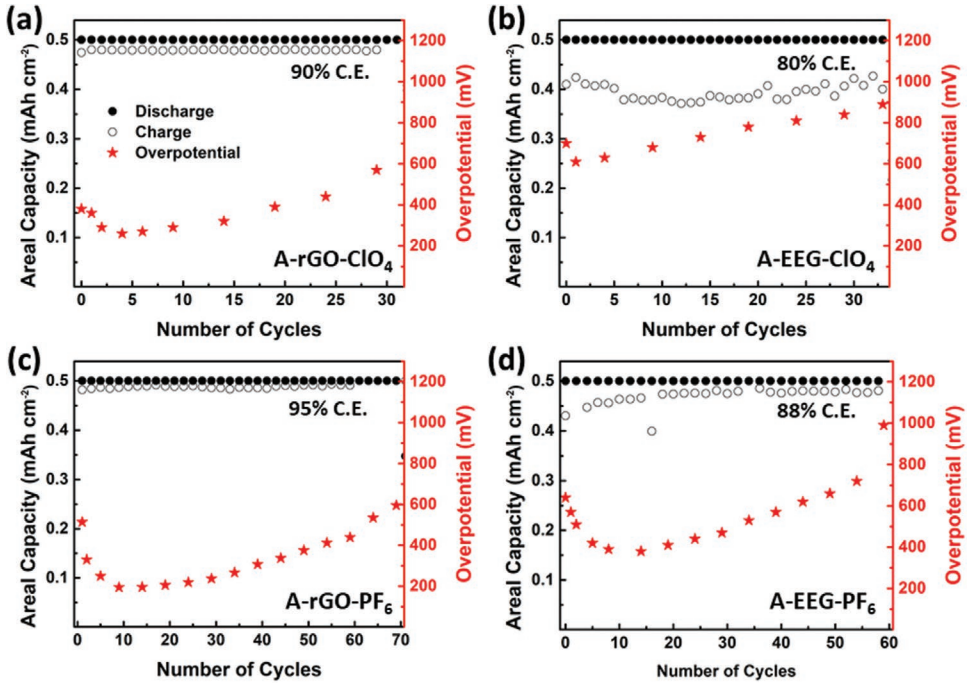

Figure 3. Evolution of discharge capacity (left axis, points denoted as filled symbols), charge capacity (left axis, points denoted as open symbols) and cell overpotential (right red axis, red stars) versus the number of cycles for a,c) A-rGO and b,d) A-EEG in 0.1 M $NaClO_4$ in DME and 0.1 M $NaPF_6$ in DME, respectively. The cell overpotential was measured at 0.2 mAh cm^{-2} for all the cells. The coulombic efficiency (C.E.) for each cathode is displayed in its respective plot.

overpotential (about 200 mV) in comparison with that of the A-rGO electrodes. Such large overpotential did not preclude A-EEG cathode from presenting a similar cycle life than that of A-rGO in both electrolytes: 34 versus 30 cycles in 0.1 M $NaClO_4$ in DME (Figure 3a,b) and 61 versus 69 cycles in 0.1 M $NaPF_6$ in DME (Figure 3c,d). The use of the $NaPF_6$-based electrolyte provided a longer cycle life, lower cell overpotential and higher efficiency for both A-rGO and A-EEG cathodes (Figure 3c,d). A noisy voltage profile, similar to that noticed in the deep-discharge experiments (Figure 2a), was recorded during the first cycles when charging the A-EEG cathode in 0.1 M $NaPF_6$ in DME (Figures S5 and S6, Supporting Information). It can therefore be concluded that A-EEG cathode yielded a larger discharge areal capacity with low discharge overpotential and longer cycle life by using 0.1 M $NaPF_6$ in DME electrolyte. Such enhanced electrochemical performance must be ascribed to AMP molecules adsorbed on the A-EEG nanosheets, as the amount and type of other oxygen-functional groups present on the surface of the A-rGO and A-EEG cathodes is very similar (compare solid traces in Figure S4a,c in the Supporting Information). However, despite its promising performance, the identified operational issues need to be addressed before this new-generation graphene could be considered as a competitive cathode material for Na–O_2 batteries. First, the large charge overpotential (Figure 3) should be reduced, as the amount of energy that a battery is able to deliver is inversely proportional to the cell potential.[38] Second, the parasitic reactions are responsible for the irregular voltage profiles when cells are fully discharge (Figure 2a, green curve) or charge in 0.1 M $NaPF_6$ in DME (Figure S5c, Supporting Information); these reactions must be therefore eliminated in order to improve the cycle life of the battery. Such operational issues are not observed when using A-rGO cathode or 0.1 M $NaClO_4$ in DME electrolyte (Figures 2a and Figure S5, Supporting Information). Hence, these phenomena seem to be related with both the use of $NaPF_6$ conducting salt and the A-EEG cathode.

We note that the occurrence of irregular voltage profiles has been already reported in aprotic metal–air batteries due to the presence of moisture in the battery cell. Water traces can induce transitory connection failures by evolution of gaseous O=PF_3 phosphate during charge.[39] Hence, it has been demonstrated that water catalyzes the oxidation of salts such as $LiPF_6$ by decomposition to PF_5^- and further formation of HF and PF_3O.[40] Concerning the discharge process, the generation of NaOH, Na_2CO_3 or $Na_2O_2{\cdot}2H_2O$ is also promoted by the presence of moisture on the cell environment. The accumulation of such products could also induce conductivity failures,[41] particularly when discharging to high capacities (Figure 2a). The build-up of these side-products can thus generate an insulating film on the cathode surface, hindering the electrical conduction throughout the electrode.[7] The discharged cathodes were studied by Raman and FTIR spectroscopies to explore the formation of amorphous side products (Figure S7, Supporting Information). The presence of NaO_2 as the major discharge product in the A-rGO cathode was verified by Raman spectroscopy. This was not the case for A-EEG, where only a faint signal related to this phase was observed after measuring several discharged cathodes (Figure S7a, Supporting Information). No bands ascribed to products other than NaO_2 were noticed in the Raman spectra for any cathode. In contrast, FTIR spectroscopy revealed the presence of $Na_2O_2{\cdot}2H_2O$ in both A-rGO and

A-EEG cathodes after discharge. The presence of other side-products, such as carbonates, carboxylates or acetates, was also apparent from the FTIR spectra, especially in the case of the A-EEG cathode (Figure S7b, Supporting Information). Unlike A-rGO cathode, A-EEG is comprised of graphene nanosheets with AMP molecules strongly adsorbed onto their surface via π–π interactions through the adenine nitrogenous base.[7] The highly hygroscopic character of the adsorbed nucleotide (conferred by its phosphorylated sugar moiety) could hinder the removal of trace water from the bulk of the electrode (even after vacuum drying at high temperature, see Experimental section), leading to the observed parasitic products and voltage fluctuations (Figure 2a and Figure S5c, Supporting Information). The proposed parasitic reactions could also affect the kinetics of the ORR and OER taking place at the cathode, thus originating large overpotentials and limiting the cycle life. Moreover, we surmise that the presence of a considerable amount of AMP molecules adsorbed on the EEG nanosheets comprising the A-EEG electrode had a strong influence on both operational issues. In order to address these challenges, the proportion of nucleotide in the A-EEG cathode was reduced by three different approaches (as detailed in the Experimental Section) to elucidate the actual role of the AMP molecules in the electrochemical performance of the battery. In a first approach, the EEG suspension was washed prior to aerogel preparation through sedimentation/resuspension cycles (A-EEG-C aerogel). In a second approach, the already prepared A-EEG aerogel was pyrolyzed under inert atmosphere at 400 °C (A-EEG-400) or 800 °C (A-EEG-800). The resulting cathodes were discharged to full capacity at 0.2 mA cm^{-2} in 0.1 M $NaPF_6$ in DME electrolyte (**Figure 4**a). A-EEG-400 and A-EEG-800 delivered a similar discharge capacity to that of the A-EEG cathode (≈6 mAh cm^{-2}, Figure 2a), while A-EEG-C yielded an areal capacity as high as 9.6 mAh cm^{-2}. The discharge overpotential of the A-EEG-400 and A-EEG-C cathodes was very similar (170–190 mV) to that of A-EEG cathode (green curve, Figure 2a). In contrast, a discharge profile with no flat plateau and a slightly higher overpotential (240 mV) was measured for A-EEG-800, which suggests an inefficient oxygen provision[42] or more limited kinetics towards the ORR.[43] Characterization of the discharged electrodes by SEM revealed a significant change in the morphology of the discharge products as function of the heat-treatment (Figure 4b–d and Figure S8, Supporting Information). While A-EEG exhibited rather small (1–4 µm) and inhomogeneous NaO_2 cubes (Figure 2e), A-EEG-400 presented more uniform and defined particles of 3–5 µm in size (Figure 4b) and A-EEG-800 displayed considerably larger products (≈30 µm, Figure 4c). However, A-EEG-800 also showed a second particle size distribution where small particles enclose the large ≈30 µm cubes. Such an observation could arise from saturation of the AMP-related active sites for the nucleation of the discharge products, so that a combination of solution-mediated and surface-mediated mechanisms would be in place for the cathodes with less amount of AMP. Hence, the prevalence of larger cubes over

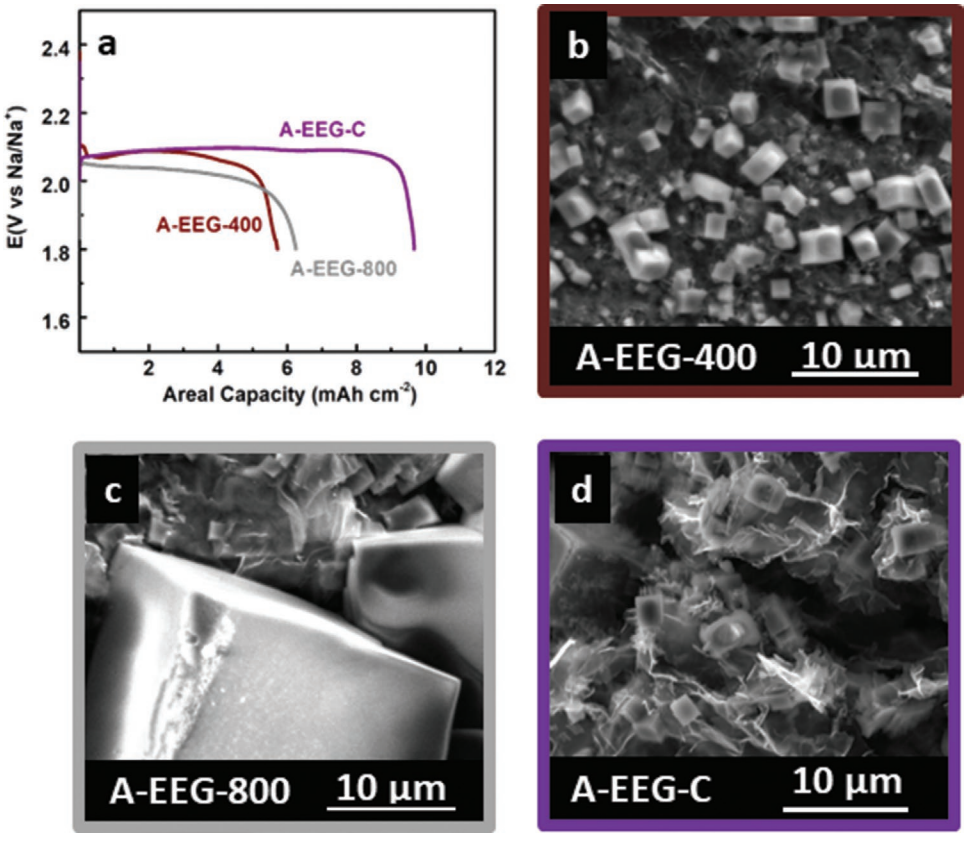

Figure 4. a) Galvanostatic deep-discharge curves of pyrolyzed (A-EEG-400 and A-EEG-800) and washed (A-EEG-C) cathodes at 0.2 mA cm^{-2} using 0.1 M $NaPF_6$ in DME electrolyte. SEM images of b) A-EEG-400, c) A-EEG-800, and d) A-EEG-C cathodes after deep discharge.

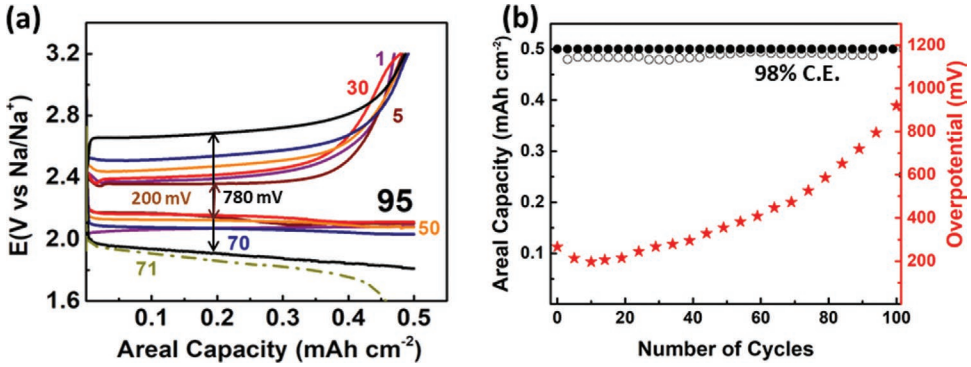

Figure 5. a) Galvanostatic charge/discharge curves at 0.2 mA cm^{-2} and b) evolution of discharge capacity (left axis, points denoted as filled symbols), charge capacity (left axis, points denoted as open symbols) and cell overpotential (right axis, red stars) versus the number of cycles for the A-EEG-C cathode. The cell overpotential was measured at 0.2 mAh cm^{-2} and the coulombic efficiency (C.E.) is displayed in plot (b).

the smallest ones in A-EEG-800 (Figure 4c and Figure S8, Supporting Information) confirms the degradation of AMP-related nucleation sites and, therefore, a possible predominance of a solution mediated mechanism. Instead of thermal degradation, the partial removal of the nucleotide by a simple washing step led to the nucleation of homogeneous ≈4 µm NaO_2 particles in the A-EEG-C cathode (Figure 4d). These results suggest a gradual shift from surface-mediated to solution-mediated discharge mechanism as the AMP molecules, adsorbed on the EEG sheets, are degraded with the pyrolysis treatment.

The cycling performance of A-EEG-400, A-EEG-800, and A-EEG-C cathodes was studied by galvanostatic charge/discharge at 0.2 mA cm^{-2} using 0.1 M $NaPF_6$ in DME electrolyte and limiting the capacity to 0.5 mAh cm^{-2}. A-EEG-400 and A-EEG-800 cathodes delivered only 10 and 5 cycles, respectively (Figure S9, Supporting Information). In contrast, A-EEG-C boasted an outstanding cycle life by delivering 95 discharge/charge cycles (**Figure 5**a,b, Supporting Information) with very low overpotential in comparison with A-rGO or A-EEG cathodes (compare Figures 3 and 5b). It must be noted that A-EEG-400, A-EEG-800 and A-EEG-C do not present any voltage noise while deep-discharging (Figure 4a) or cycling (Figure 5a and Figure S9, Supporting Information). In addition, the cell overpotential decreased significantly for all of them, particularly for the A-EEG-C cathode, where an overpotential value of only 260 mV was observed in the first cycles (Figure S9c, Supporting Information). The parasitic reactions occurring for A-EEG cathode seemed to be suppressed when the amount of AMP was reduced by thermal treatment or washing. Indeed, the FTIR spectroscopy analysis of the discharged A-EEG-C and A-EEG-800 electrodes revealed that formation of side-products was considerably reduced when the amount of AMP molecules adsorbed on the graphene aerogel surface was decreased (Figure S7b, Supporting Information).

The discharge capacity and the cyclability values delivered by A-EEG-C are very significative and, therefore, our approach comprises the comparison of this cathode with other carbon-based electrode materials. Table S1 (Supporting Information) summarizes some of the most representative cathode materials (including catalysts, carbon-based or graphene-based materials) reported for Na–O_2 batteries. Critical parameters such as mass loading or areal capacity have been considered for a fair comparison between the state-of-art and the present work. It can be first noticed that most reported works show an extremely low mass loading (0.3–0.8 mg cm^{-2})[16–22,23] when compared to the present study (3.15 mg cm^{-2}). Moreover, in some cases, capacity and current density values are calculated only on the basis of the carbon weight, which varies from 90% to 60% of the total electrode mass, due to the addition of binder and/or catalysts, which result in a considerable overestimation of the cell capacity.[17,20,22] In addition, complex synthetic procedure[14,18,20,22] and toxic or expensive materials (Co, Ru) are employed,[14,16,17,21] which considerably hinders its large scale production and commercialization. Besides these facts, only two works reported similar deep discharge areal capacities (8.8 and 9.1 mAh cm^{-2}),[21,23] however, the current densities applied (0.12–0.13 mA cm^{-2}) are two times lower than that used in the present work (0.2 mA cm^{-2}). Concerning cyclability, the previous studies reported a cycle life between 80 and 160 charge/discharge cycles; however, the applied current density (0.045–0.1 mA cm^{-2})[13,16,17,19,20] or the capacity limitation values (0.15–1 mAh cm^{-2})[14,18,21–23] were much lower than those found in the present work. Specifically, the work reported by Zhao et al. using VACNTs displayed 100 cycles at 0.1 mA cm^{-2} to 1 mAh cm^{-2}. This work applies a lower cycling rate (0.1 vs 0.2 mA cm^{-2}) but at a larger capacity (1 vs 0.5 mAh cm^{-2}).[13] Carbon–ruthenium composites[14] delivered 110 cycles at similar current density and capacity cut off but the mass loading was not specified and the cell overpotential was extremely high (1.1 V). Boron doped carbon cathodes[18] or printed 3D graphene cathodes[23] also delivered ≈120 cycles at high current density (0.3 mA cm^{-2}) but the capacity limitation and the mass loading are lower than A-EEG-C cathode (Table S2, Supporting Information). Finally, porous carbon nanospheres delivered 400 cycles at similar current densities, capacity cut-off and cell overpotential but the mass loading was 10 times lower than the present work (0.3 vs 3.15 mg cm^{-2}). Considering these results, it can be concluded that A-EEG-C electrodes are highly competitive with those reported in literature for Na–O_2 cathode materials. Moreover, the development of cathode materials incorporating catalytically active and innocuous biomolecules opens up a new avenue for the development of more ecofriendly and high-performing Na–O_2 batteries; which is a field yet to be explored.[44]

3.3. Elucidating the Role of AMP Nucleotide on Battery Performance

An in deep understanding of the phenomena enhancing the performance of A-EEG-C electrode will provide tools to rationalize the future design of Na–O_2 cathodes, pushing the limits of efficient energy storage. The structure and the surface chemistry, as well as the decomposition behavior, of the aerogels tested in Section 3.2 were comprehensively studied in order to understand their different electrochemical behavior. The inspection of all the pristine graphene aerogel cathodes by SEM (Figure S8, Supporting Information) revealed some morphological differences which might contribute to their different cycling performance. Similar to A-EEG, the pyrolyzed aerogels presented a highly aggregated morphology but, in this case, a more opened structure with visible voids in-between highly twisted graphene sheets was observed. In contrast, the morphology of A-EEG-C was more similar to that of A-rGO aerogel, where smooth and slightly wrinkled sheets with large voids in-between were verified. An increase of the porosity with the removal of the AMP molecule from the surface of the aerogels was further confirmed by comparison of the N_2 isotherms (Figure S10, Supporting Information). The increase of the porosity is not significant for the pyrolyzed aerogels (A-EEG-400 and A-EEG-800) but the A-EEG-C aerogel presented much developed porosity, which was nearly equivalent to that in the rGO cathode (Table S1, Supporting Information). We therefore hypothesize that the structural integrity of the EEG-derived aerogels is largely provided by the AMP molecules, which act as a sort of "biomolecular glue" between neighboring graphene nanosheets. The origin of this effect can be ascribed to the well-known ability of nucleotides to establish a variety of hydrogen bonding interactions.[45] In such a scenario, an AMP molecule adsorbed on a given EEG nanosheet could easily attach to another AMP molecule adsorbed on a close-by nanosheet by the formation of hydrogen bonds, thus providing structural integrity to the nanosheet assembly in the EEG aerogel. The decomposition of the nucleotide in the aerogel by pyrolysis could remove this "biomolecular glue" effect leading to the restack/twisting of the EEG sheets and, consequently, to the collapse of the 3D porous structure on A-EEG-400 and A-EEG-800 materials. Indeed, the morphology of the heat-treated aerogels by SEM imaging changed substantially as compared with A-EEG (Figure S8, Supporting Information) but, in contrast, the morphology of the graphene sheets is similar in all A-EEG-derived aerogels (see TEM images in Figure S2 in the Supporting Information after fragmentation of aerogels to get suitable specimens). Hence, we hypothesize that their poor cycle life (Figure S9, Supporting Information) is ascribed, at least in part, to this phenomenon, where the diffusion of oxygen and electrolyte molecules is no longer facilitated within the cathode structure. In this regard, the removal of the nucleotide through a simple washing step seems to be the best option to preserve a stable porous 3D structure on the EEG-derived cathodes (Figures S8 and S10, Supporting Information). This effect is not observed for common rGO cathodes as the assembly mechanism for GO sheets is different from that in less-defective EEG sheets (Figure 1c). The pyrolysis of the GO aerogel provides the material with enlarged structural stability as the elimination of oxygen functionalities existing on the surface of the sheets generates a large amount of unsaturated carbon atoms on the basal plane. These highly reactive atoms can interact each other to form covalent bonds between neighboring sheets to conform a robust 3D structure.[34] Despite of the commented changes on the morphology/structure of the A-EEG aerogels, the chemical changes associated to the decomposition of the AMP nucleotide on the pyrolyzed cathodes should be also considered to explain the differences on the discharge mechanism and the decay of the cycling performance. With this aim, the materials were studied by TGA under inert atmosphere, i.e., under similar conditions to those investigated in the pyrolysis treatments. The first bond scissions in the nucleotide are expected to occur on the most thermolabile bonds of the molecule (**Figure 6**a), namely, the phosphoester bond between the ribose and the phosphate, as well as the C—N linkage between the ribose and the adenine nucleobase.[46] For comparative purposes, the thermal degradation of pure AMP powder was also monitored (Figure 6b). The thermogravimetric profile of pure AMP revealed three well-resolved events: i) an initial weight loss taking place up to 170 °C, ii) a marked weight loss at ≈240–300 °C, and iii) a gradual, slow weight loss up to 1000 °C. The first event can be ascribed to the release of adsorbed water molecules[47] from the highly hygroscopic AMP powder (Figure S11, Supporting Information), while the other two events corresponded to the degradation of the nucleotide molecule. It has been reported that sugar-like compounds (including ribose) melt/decompose within the 185–300 °C temperature range.[48–51] Hence, the release of low molecular weight gaseous products (such as CO_2, H_2O, or CH_4) from the decomposition of the ribose moiety in AMP probably causes the marked weight loss at ≈240–300 °C (Figure 6b). Right after ribose decomposition, both phosphoric acid and adenine will be left behind, with the condensation of phosphoric acid to give long-chain polyphosphates occurring for temperatures above 200–300 °C,[52,53] the decomposition of the nucleobase at around 350 °C[54] and preservation of polyphosphates as not volatile residues at high temperatures.[53] Bearing this in mind, the weight loss observed at temperatures between ≈300 and ≈800 °C might result from the volatilization of nitrogen-containing compounds, such as NH_3HCN or HCNO[54–56] (adenine decomposition), and the release of water induced by phosphates condensation. The A-EEG and A-EEG-C aerogels also displayed rather similar decomposition profiles, especially when compared to that of pure AMP powder (Figure 6b). Nevertheless, the weight loss assigned to ribose decomposition shifted to lower temperatures for the aerogels (≈150–200 °C). The early decomposition of ribose when the nucleotide is adsorbed onto the surface of EEG sheets was further confirmed by monitoring the decomposition of A-EEG-200. This material, which was obtained by drying the A-EEG aerogel under the same conditions as cathodes prior to the Na–O_2 cell assembly (see the Experimental Section), did not display any marked weight loss ≈150–200 °C (Figure 6b). The high thermal conductivity of the graphene nanosheets in the aerogels could accelerate the heat transfer to the adsorbed AMP molecules, leading to the decomposition of ribose moiety in the dried cathodes (temperatures ≤ 200 °C). The total weight losses recorded at 1000 °C for A-EEG (47 wt%) and A-EEG-C (41 wt%) were similar, suggesting that the nucleotide molecules were strongly adsorbed to the graphene surface and thus were

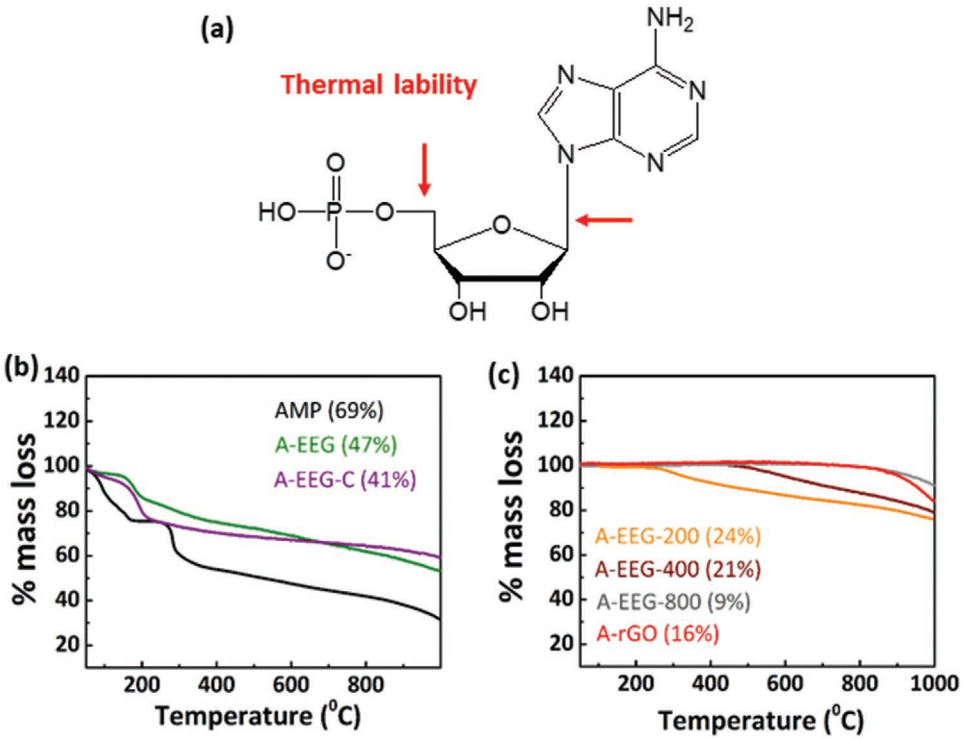

Figure 6. a) Chemical structure of AMP with its most labile bonds highlighted. b) Thermogravimetric profiles of pure AMP powder, A-EEG and A-EEG-C, and c) heat-treated graphene aerogels A-rGO, A-EEG-400, and A-EEG-800. The total weight loss (wt%) is specified for each sample.

difficult to remove by the washing procedure. In contrast, the pyrolyzed aerogels (i.e., A-EEG-400, A-EEG-800, and A-rGO) displayed very flat TGA profiles and lower mass losses (9–21 wt%, Figure 6c), which was due to the prior decomposition of the nucleotide from the EEG-based aerogels and the removal of most of the oxygen functional groups from the GO nanosheets for the A-rGO aerogel. A-EEG-400 displayed a gradual weight loss above 400 °C, as it should have partially preserved the adenine and/or short-chain phosphates on the surface of the graphene nanosheets. Despite of the strong hygroscopic character of the pure AMP molecule (Figure S11, Supporting Information) the water adsorption seems not to be so extensive on either A-EEG or A-EEG-C aerogels, where the weight loss registered by TGA at low temperatures was much smaller than that recorded for the pure nucleotide (Figure 6b). The aerogels subjected to heat treatment (A-rGO, A-EEG-400, and A-EEG-800) did not show, as expected, any appreciable water release (Figure 6b).

For further inspection of the hydrophilic character of the most representative cathode materials, the A-rGO, A-EEG-C, and A-EEG aerogels were dried under vacuum at 200 °C for 12 h and transferred to the agon glove box with no exposure to the environment. Each aerogel (3 mg) was immersed in 2 mL of fresh DME for 4 days, and then the content of water in the organic solvent was measured by titration with a coulometer. The water content of the solutions of fresh DME, A-rGO, A-EEG-C, and A-EEG was 3.5, 8.4, 9.2, and 14.5 ppm, respectively. This result further supported the idea that trace water participated in the formation of side-products and voltage noise during the deep-discharge/cycling of the A-EEG cathode (Figures 2a and Figure S5c, Supporting Information).

The thermal degradation mechanism of the AMP molecules adsorbed on EEG-derived graphene aerogels was also investigated by XPS analysis. The high-resolution core level spectra of the elements of interest is displayed in **Figure 7**. The presence of pristine AMP molecules adsorbed on the surface of A-EEG and A-EEG-C aerogels was evidenced by the calculation of the P:N atomic ratio from the atomic compositions gathered in **Table 2**. Hence, the P:N ratio for A-EEG and A-EEG-C were quite similar to that predicted from the empirical formula of AMP molecule (1:5) while the heat-treated samples showed much lower values. Furthermore, the high resolution N 1s core level spectra (Figure 7a) of A-EEG and A-EEG-C exhibited the features expected for the pristine AMP molecule, i.e., two components at binding energies (BEs) of ≈399.1 and ≈400.5 eV in an ≈3:2 ratio, which correspond to imine- and amine-type nitrogen in AMP molecule, respectively.[57] The P 2p and O 1s spectra were also qualitatively similar for A-EEG and A-EEG-C. The presence of phosphate-like functionalities in both materials was revealed by a doublet P 2p band (Figure 7b) with P $2p_{3/2}$ and P $2p_{1/2}$ components centered at ≈133.2 and 134.1 eV, respectively. An intense band centered at ≈532.5 eV in the O1s spectra (Figure 7c) suggested the existence of C—O—P, C—O—C, and C—OH bonds and, consequently, the existence of the ribose moiety on the adsorbed adenine molecules. The shoulder at ≈531.0 eV is assigned to C=O as well as to terminal P=O and P—OH bonds in phosphates which confirms the existence of short-chain orthophosphates in the aerogels not subjected to thermal treatment. Concerning the C 1s spectra (Figure 7d), A-EEG and A-EEG-C displayed two main components centered at ≈284.5 and ≈286.6 eV, which corresponded to

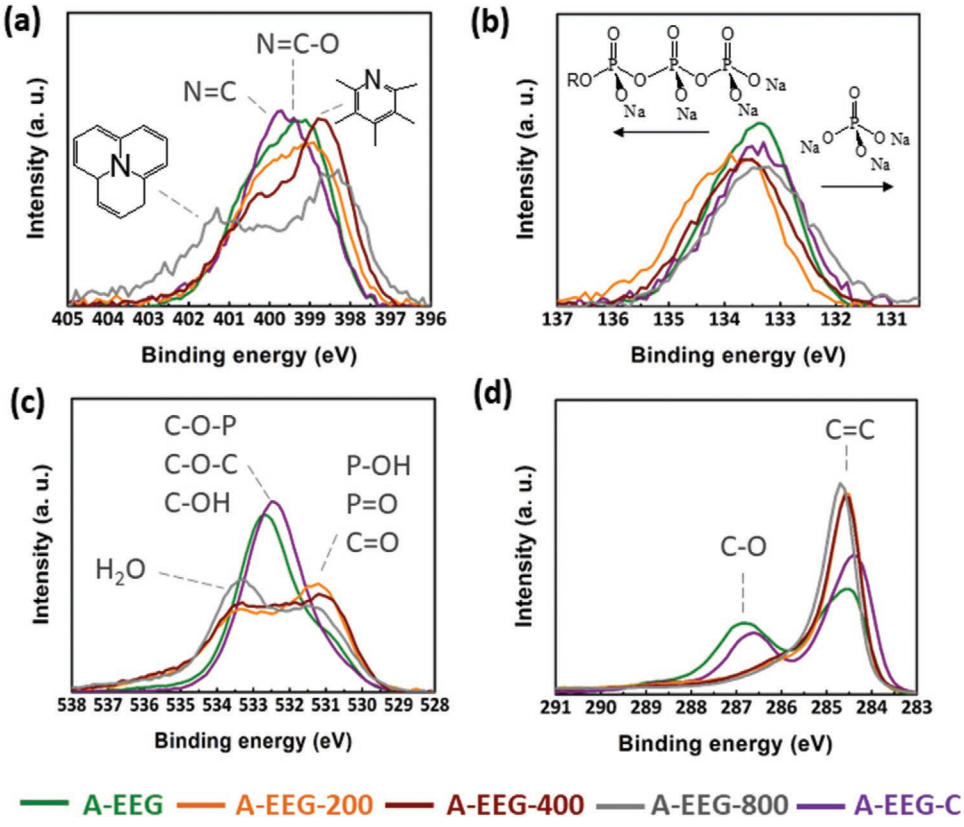

Figure 7. Background-subtracted and normalized high-resolution a) N 1s, b) P 2p, c) O 1s, and d) C 1s XPS spectra of the different EEG-based aerogels.

C=C structures in the graphene lattice and to carbon single-bonded to heteroatoms (C—O and C—N), respectively. The relative contribution of the C—O component at ≈286.6 eV to the overall C 1s band was clearly smaller for the A-EEG-C aerogel, indicating that the washing step removed part of the AMP content. Even though the contribution of C—O bonds could also arise from the oxygen groups existing on the graphene sheets itself and not only belong to the adsorbed AMP molecules, the sharp decrease in both P and N content of A-EEG-C compared to A-EEG (Table 2) confirms the efficiency of washing the EEG sheets in removing part of the AMP molecules from the surface of the A-EEG-C aerogel. The vacuum-drying of the aerogel cathode (A-EEG-200) did not originate any changes on the shape of the high-resolution N 1s spectrum (Figure 7a) compared to that of A-EEG and A-EEG-C. In contrast, the bands assigned to C—O structures in both the O 1s and C 1s spectra, as well as the oxygen content in Table 2, dropped dramatically for A-EEG-200 (Figures 7c,d). In accordance with the TGA analysis, both phenomena confirmed the decomposition of the oxygen-rich ribose moiety and the preservation of the nitrogenated nucleobase on the AMP molecule for temperatures ≤ 200 °C. Regarding pyrolyzed samples, the treatment of A-EEG to temperatures ≥ 400 °C (A-EEG-400) led to the decomposition of the adenine moiety and, consequently, to the emergence of new components in the N 1s spectra (Figure 7a), which were assigned to nitrogen inserted into the sp^2-based carbon lattice. Specifically, the A-EEG-400 N 1s spectrum displayed an intense band related to pyridine-type nitrogen located at the edge of the graphene sheets (BE of ≈398.5 eV), while the A-EEG-800 spectrum could be fitted to a combination of pyridinic and quaternary nitrogen inserted on the carbon lattice at the basal plane (BE of ≈401.1eV). The presence of this new type of species on the pyrolyzed samples can arise from the incorporation of nitrogen into the graphene lattice, as this can result from the reaction of nitrogen-containing compounds derived from adenine decomposition with oxygen functional groups in the EEG nanosheets.[58,59] As well, the extensive decomposition of the nucleotide in A-EEG-400 and A-EEG-800 is expected to yield a doped (i.e., containing nitrogen and phosphorus) carbon residue that will integrate into the EEG-based aerogel.[60] In this sense, the atomic proportion of phosphorus remains inalterable for all the pyrolyzed aerogels (Table 2), which confirms

Table 2. Surface composition for all the graphene aerogels in at% determined from the high-resolution core level spectra of the elements of interest. The samples subjected to thermal treatment are highlighted in gray.

	P:N ratio	C [at%]	O [at%]	N [at%]	P [at%]
A-EEG	1:4.2	67.66	23.91	6.8	1.63
A-EEG-C	1:4.9	76.26	19.81	3.27	0.66
A-EEG-200[a)]	1:3.8	82.28	11.31	5.09	1.32
A-EEG-400[b)]	1:2.3	83.63	9.90	4.50	1.97
A-EEG-800[b)]	1:1.8	84.63	11.51	2.48	1.38

[a)]Dried in vacuum at 200 °C for 12 h emulating the drying conditions of the cathodes prior to cell assembly; [b)]Treated under pyrolytic conditions under nitrogen flow at different temperatures.

the retention of phosphates as nonvolatile residues at high temperatures. The width of the P 2p band (FWHM) in Figure 7b increased gradually from 1.7 eV for A-EEG-200 to 2.2 eV for A-EEG-800 by increasing the treatment temperature. This phenomenon reveals an increasing heterogeneity of the phosphorus chemical environment as the temperature of the treatment increases and, therefore, is compatible with the presence of phosphates and/or polyphosphates in the aerogels treated at higher temperatures.[61] Indeed, the condensation of phosphates induced by pyrolysis is a well-documented fact[53,62] and, therefore, the presence of polyphosphates in A-EEG-400 and A-EEG-800 is highly likely. In contrast, phosphorus appeared exclusively as phosphate in A-EEG, A-EEG-200, and A-EEG-C as these materials were not subjected to pyrolysis at high temperature. Concerning oxygen, the heating of A-EEG aerogel to temperatures above 200 °C did not lead to significant changes on the C—O related bands in both the O 1s and C 1s spectra as compared to the dramatic drop of observed in A-EEG-200 (Figure 7c,d). Thus, the O:C atomic ratio of A-EEG-200, A-EEG-400, and A-EEG-800 was similar regardless of the heat treatment temperature (≈0.12–0.14, as calculated from their surface composition in Table 2). It can be concluded that drying the aerogel cathodes under vacuum at 200 °C for 12 h produced the decomposition of the oxygen-rich ribose moiety but conserve the phosphate and adenine moieties. The pyrolysis of the A-EEG aerogel to temperatures above 400 °C causes i) the adenine decomposition to yield a doped carbon residue on the top of the EEG sheets and/or the functionalization/doping of the carbon basal plane and ii) the partial condensation of phosphates to give polyphosphate species.

From the results presented above, several remarks can be made about the important role of AMP in the performance of the EEG-based aerogels in Na–O_2 batteries. First, we note that AMP molecules are strongly adsorbed on the EEG nanosheets that comprise the aerogels. This can be deduced from the observation that even after extensive washing (EEG-C suspension), the EEG nanosheets were still colloidally stable in the aqueous medium, which can only be the result of a rather strong interaction between the AMP molecules and the nanosheets.[31] In turn, such a strong adsorption implies that AMP will make up a sizable fraction of the total weight of the resulting aerogels (roughly estimated to be between a few and several tens wt% from the TGA and XPS data). The large amount of electrically insulating AMP present in the aerogels hinders, to a certain extent, their electrical conductivity, particularly in the case of aerogels derived from nonextensively washed EEG dispersions, which was probably the origin of the large cell overpotential found for the A-EEG cathodes (Figure 3). This problem is alleviated to some extent when using the thoroughly washed (and thus less AMP-laden) EEG-C suspensions, as actually observed from the behavior of the corresponding A-EEG-C cathode (Figure 5). Furthermore, a lower amount of hygroscopic AMP in the aerogels facilitates their drying, leading to lower levels of trace water in the cathodes (as indeed measured here for A-EEG-C vs A-EEG by coulometric titration) and enhancing the battery performance by minimizing the parasitic reactions (Figure 4a; Figures S7 and S9, Supporting Information). A similar effect can take place when AMP is decomposed by pyrolysis at medium-high temperatures (A-EEG-400 and A-EEG-800 cathodes), as the resulting carbonaceous residue[60] is expected to be electrically conductive and relatively hydrophobic. Nevertheless, the cycle life of the A-EEG-400 and A-EEG-800 cathodes was seriously affected (Figure S9, Supporting Information), probably due to the modification of the porosity, the morphology and the surface chemistry of the aerogel material. Concerning the chemistry of the cathode, the pyridinic/quaternary nitrogen existing on the carbon residue generated after adenine decomposition on A-EEG-400 and A-EEG-800 (Figure 7a) could act as catalytic sites for the ORR and OER reactions. Indeed, the electrocatalytic activity of pyridinic and quaternary-like nitrogen in graphitic structures towards ORR/OER reactions has been widely reported both in aqueous[63–69] and organic media.[70,71] Bearing this in mind, the decay of the cycle life on A-EEG-400 and A-EEG-800 might be therefore ascribed to a decreased diffusion of oxygen/electrolyte molecules towards the nitrogen-containing electroactive catalytic sites in the cathode,[25] promoted by the collapse of the 3D porous structure. Thus, AMP probably acts as a linker between the EEG nanosheets in the aerogels, providing them with porosity and some structural integrity where the decomposition of the nucleotide by pyrolysis led to aerogel collapse (Figure S8 and S10, Supporting Information).

Likewise nitrogen-doped carbon materials, organic molecules that incorporate imine-like nitrogen sites (including adenine, Figure 7a) have also demonstrated a high electrocatalytic activity towards ORR/OER reactions when supported onto graphitic/graphenic carbon materials.[72–74] In this sense, the adenine molecules adsorbed on both A-EEG-C cathodes can also present a high electrochemical activity on both discharge (ORR) and charge (OER) throughout the Na–O_2 battery cycling. The conservation of the AMP molecule as "assembler" in A-EEG-C further provides the cathode with an open porous structure (Figure S8, Supporting Information) and, consequently, with highly accessible nitrogen catalytic sites to achieve an enhanced cycling performance.

The role of the phosphate present in AMP on the discharge mechanism of Na–O_2 batteries was proposed in our previous work.[7] Mainly, a proportion of the superoxide molecules (O_2^-) that are generated during ORR interact with protonated orthophosphates on the surface of the EEG-based aerogel to form an intermediate (—C—PO_2—O—H—O_2, **Figure 8**a) thus promoting the nucleation and growth of nanometer-sized NaO_2 particles (Figures 2e and 4d) via a surface-mediated mechanism. This interaction can also facilitate the redissolution of NaO_2 cubes into molecular oxygen (OER) by stabilization of the superoxide intermediates by interaction with the orthophosphates during charge. In the present work, this hypothesis is reinforced as the partial condensation of orthophosphates to give polyphosphates in A-EEG-400 and A-EEG-800 could be also responsible for their poor cycling performance. Hence, the polymerization of orthophosphates on the pyrolyzed aerogels leads to a substantial reduction in the number of terminal P—OH acidic sites, so that the ability of these cathodes to retain the O_2^- species on their surface will be markedly decreased relative to that of A-EEG and A-EEG-C. In the case of A-EEG and A-EEG-C, ORR is catalyzed by adenine itself on the cathode surface, where its reduced counterpart (O_2^-) will interact with the terminal oxygen atoms in the neighboring orthophosphates (Figure 8a). In this case, the migration of Na^+ from the electrolyte to the cathode

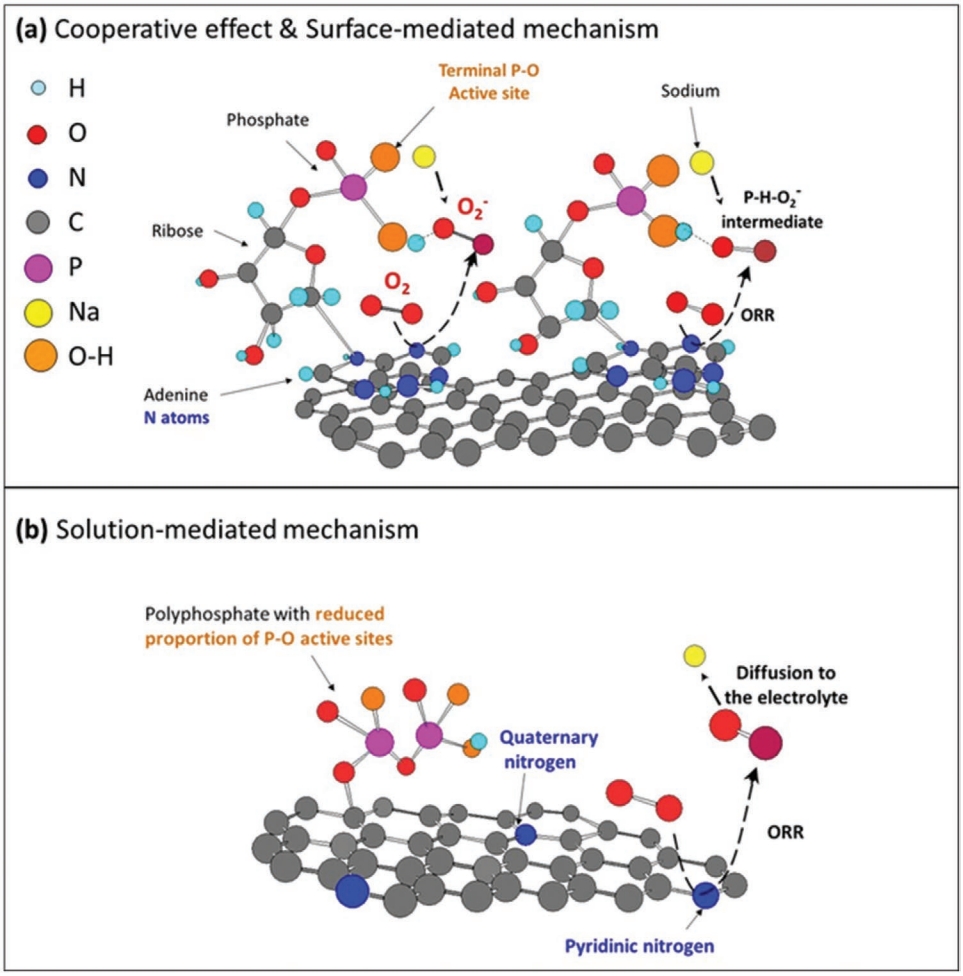

Figure 8. Schematic illustration of the proposed discharge mechanism as a function of the surface chemistry of the different EEG-derived aerogels. a) Cooperative effect between nitrogen of adenine and the phosphate group in AMP promoting the surface-mediated mechanism. b) Solution-mediated mechanism for aerogels pyrolyzed at high temperature, where polymerization of phosphate groups into polyphosphates decreases the ability of the aerogel surface to retain the superoxide (O_2^-) anion.

surface to recombine with the "trapped" superoxide anions will promote the nucleation of small NaO_2 cubes via surface-mediated mechanism. In contrast, the decrease of P-OH-like O_2^- binding sites (Figure 8b) on the surface of both A-EEG-400 and A-EEG-800 cathodes will increase the diffusion of O_2^- species into the bulk of the electrolyte to recombine with Na^+, promoting the solution-mediated mechanism and thus leading to the formation of larger NaO_2 particles (Figure 4b,c). We note that drying the graphene cathodes under vacuum at 200 °C for 12 h led to (at least partial) decomposition of the ribose moiety in the adsorbed AMP molecules, but did not result in any detrimental effect on the cathode performance as both the adenine and orthophosphate species are conserved. Thus, the high performance of the A-EEG-C cathode can be ascribed to a possible cooperative effect between the adenine nucleobase and the orthophosphate from AMP (Figure 8a). Specifically, the adenine acts as a catalyst for the ORR and OER reactions while phosphates act as anchor sites for the reduced superoxide species (O_2^-), favoring the growth or dissolution of NaO_2 products during the discharge and charge, respectively.

4. Conclusions

The performance of graphene aerogel cathodes for Na–O_2 batteries—prepared by a straightforward, potentially scalable and sustainable nucleotide-assisted electrochemical method- was compared with that of more conventional cathodes based on reduced graphene oxide in different glyme-based electrolytes. The electrochemically exfoliated graphene aerogels presented enhanced discharge capacity and similar cycle life to that of rGO cathodes in both 0.1 M $NaPF_6$ DME and 0.1 M $NaClO_4$ DME electrolytes. The use of $NaPF_6$ conducting salt resulted in a considerable increase of the cycle life, efficiency and discharge capacity for both cathode materials. An excessive amount of the nucleotide (adenosine monophosphate, AMP) in the electrochemical exfoliated graphene cathode led to irregular discharge/charge profiles and large overpotentials, probably associated to the detrimental effect of the biomolecule on the electrical conductivity and the introduction of moisture/parasitic reactions into the cell. Nevertheless, control of both the chemical state and the amount of the nucleotide present in the aerogels addressed the

above-mentioned operational issues. Hence, the removal of a fraction of the nucleotide molecules adsorbed onto the graphene sheets by a proper washing step prior to their assembly into a 3D aerogel led to an outstanding cycle life of almost 100 cycles at the relatively high current density of 0.2 mA cm^{-2}. In addition, a discharge capacity as large as 9.6 mAh cm^{-2} was retained while the cell overpotential was considerably reduced. Treatment of the graphene aerogel at different temperatures under inert atmospheres provided highly relevant knowledge on the role of specific moieties from the AMP molecule in the cathode performance. In addition, the nitrogen-containing nucleobase and the acidic P—OH sites in orthophosphates from AMP work cooperatively to promote the nucleation of NaO_2 during discharge while enhancing its dissolution during charge. The crucial role of the AMP molecules on the assembly of the low-defect electrochemically exfoliated graphene sheets was also made evident by the collapse of the aerogel structure upon nucleotide degradation; the catalytic nucleobase and acidic sites were no longer accessible to the oxygen and electrolyte molecules. Finally, a better understanding of the altered mechanism occurring at the graphene cathode by the presence of this AMP nucleotide has resulted in 1) improved performance values when compared with those reported and 2) a new avenue of research into future investigation of bio-inspired cathode materials for metal–oxygen batteries.

Supporting Information

Supporting Information is available from the Wiley Online Library or from the author.

Acknowledgements

M.E., J.L.G.-U., D.C., and N.O.-V. thank the European Union (Graphene Flagship-Core 3, Grant number 881603) and the Spanish Ministry of Science and Innovation (MICINN/FEDER) (RTI2018-096199-B-I00) for the financial support of this work. J.M.M., J.I.P., and S.V.-R. gratefully acknowledge funding by the Spanish Ministerio de Ciencia, Innovación y Universidades (MICINN), Agencia Estatal de Investigación (AEI), and the European Regional Development Fund (ERDF) through project RTI2018-100832-B-I00, as well as Plan de Ciencia, Tecnología e Innovación (PCTI) 2013-2017 del Principado de Asturias and the ERDF (project IDI/2018/000233). J.L.G.-U. is very thankful to the Spanish Ministry of Education, Science and Universities (MICINN) for the FPU grant (16/03498). The authors also want to acknowledge the company GRAPHENEA for supplying the graphene oxide used in this work. The authors express special thanks to María Echeverría for SEM imaging and María Jauregui for XRD measurements.

Conflict of Interest

The authors declare no conflict of interest.

Keywords

catalysis, cathode, glyme-based electrolytes, graphene, Na–air batteries, nucleotides

Received: August 17, 2020
Revised: November 10, 2020
Published online:

[1] U. Salahuddin, H. Ejaz, N. Iqbal, *Int. J. Energy Res.* **2018**, *42*, 2021.
[2] W. Tahil, *The Trouble with Lithium. Implications of Future PHEV Production for Lithium Demand: Meridian International Research*. Martainville **2007**, http://www.meridian-int-res.com/Projects/Lithium_Problem_2.pdf.
[3] L. Lutz, W. Yin, A. Grimaud, D. Alves Dalla Corte, M. Tang, L. Johnson, E. Azaceta, V. Sarou-Kanian, A. J. Naylor, S. Hamad, J. A. Anta, E. Salager, R. Tena-Zaera, P. G. Bruce, J. M. Tarascon, *J. Phys. Chem. C* **2016**, *120*, 20068.
[4] H. Yadegari, Y. Li, M. N. Banis, X. Li, B. Wang, Q. Sun, R. Li, T. K. Sham, X. Cui, X. Sun, *Energy Environ. Sci.* **2014**, *7*, 3747.
[5] N. Mahne, O. Fontaine, M. O. Thotiyl, M. Wilkening, S. A. Freunberger, *Chem. Sci.* **2017**, *8*, 6716.
[6] F. Wu, Y. Xing, J. Lai, X. Zhang, Y. Ye, J. Qian, L. Li, R. Chen, *Adv. Funct. Mater.* **2017**, *27*, 1700632.
[7] J. M. Munuera, J. I. Paredes, M. Enterría, S. Villar-Rodil, A. G. Kelly, Y. Nalawade, J. N. Coleman, T. Rojo, N. Ortiz-Vitoriano, A. Martínez-Alonso, J. M. D. Tascón, *ACS Appl. Mater. Interfaces* **2020**, *12*, 494.
[8] H. Yadegari, C. J. Franko, M. N. Banis, Q. Sun, R. Li, G. R. Goward, X. Sun, *J. Phys. Chem. Lett.* **2017**, *8*, 4794.
[9] H. Yadegari, X. Sun, *Acc. Chem. Res.* **2018**, *51*, 1532.
[10] X. Lin, Q. Sun, K. D. Davis, R. Li, X. Sun, *Carbon Energy* **2019**, *1*, 141.
[11] R. C. Alkire, P. N. Bartlett, J. Lipkowski, *Electrochemistry of Carbon Electrodes*, Wiley, New York **2015**.
[12] P. Lou, C. Li, Z. Cui, X. Guo, *J. Mater. Chem. A* **2015**, *4*, 241.
[13] N. Zhao, C. Li, X. Guo, *Phys. Chem. Chem. Phys.* **2014**, *16*, 15646.
[14] J. H. Kang, W. J. Kwak, D. Aurbach, Y. K. Sun, *J. Mater. Chem. A* **2017**, *5*, 20678.
[15] Y. Hu, X. Han, Q. Zhao, J. Du, F. Cheng, J. Chen, *J. Mater. Chem. A* **2015**, *3*, 3320.
[16] Y. Liu, X. Chi, Q. Han, Y. Du, J. Yang, Y. Liu, *J. Alloys Compd.* **2019**, *772*, 693.
[17] N. Li, Y. Yin, F. Meng, Q. Zhang, J. Yan, Q. Jiang, *ACS Catal.* **2017**, *7*, 7688.
[18] C. Shu, Y. Lin, B. Zhang, S. B. Abd Hamid, D. Su, *J. Mater. Chem. A* **2016**, *4*, 6610.
[19] J. L. Ma, X. B. Zhang, *J. Mater. Chem. A* **2016**, *4*, 10008.
[20] S. Zhang, Z. Wen, J. Jin, T. Zhang, J. Yang, C. Chen, *J. Mater. Chem. A* **2016**, *4*, 7238.
[21] J. L. Ma, F. L. Meng, D. Xu, X. B. Zhang, *Energy Storage Mater.* **2017**, *6*, 1.
[22] B. Sun, K. Kretschmer, X. Xie, P. Munroe, Z. Peng, G. Wang, *Adv. Mater.* **2017**, *29*, 1606816.
[23] X. Lin, J. Wang, X. Gao, S. Wang, Q. Sun, J. Luo, C. Zhao, Y. Zhao, X. Yang, C. Wang, R. Li, X. Sun, *Chem. Mater.* **2020**, *32*, 3018.
[24] J. L. Gómez Urbano, M. Enterría, I. Monterrubio, I. Ruiz de Larramendi, D. Carriazo, N. Ortiz-Vitoriano, T. Rojo, *ChemSusChem* **2019**, *13*, 1203.
[25] M. Enterría, C. Botas, J. L. Gómez-Urbano, B. Acebedo, J. M. López Del Amo, D. Carriazo, T. Rojo, N. Ortiz-Vitoriano, *J. Mater. Chem. A* **2018**, *6*, 20778.
[26] J. Chen, B. Yao, C. Li, G. Shi, *Carbon* **2013**, *64*, 225.
[27] P. P. Brisebois, M. Siaj, *J. Mater. Chem. C* **2020**, *8*, 1517.
[28] J. I. Paredes, J. M. Munuera, *J. Mater. Chem. A* **2017**, *5*, 7228.
[29] A. J. Patil, J. L. Vickery, T. B. Scott, S. Mann, *Adv. Mater.* **2009**, *21*, 3159.
[30] J. I. Paredes, S. Villar-Rodil, P. Solís-Fernández, A. Martínez-Alonso, J. M. D. Tascón, *Langmuir* **2009**, *25*, 5957.
[31] M. Ayán-Varela, J. I. Paredes, L. Guardia, S. Villar-Rodil, J. M. Munuera, M. Díaz-González, C. Fernández-Sánchez, A. Martínez-Alonso, J. M. D. Tascón, *ACS Appl. Mater. Interfaces* **2015**, *7*, 10293.
[32] P. Solís-Fernández, J. I. Paredes, S. Villar-Rodil, A. Martínez-Alonso, J. M. D. Tascón, *Carbon* **2010**, *48*, 2657.
[33] Y. Xu, Q. Wu, Y. Sun, H. Bai, G. Shi, *ACS Nano* **2010**, *4*, 7358.
[34] R. Rozada, J. I. Paredes, S. Villar-Rodil, A. Martínez-Alonso, J. M. D. Tascón, *Nano Res.* **2013**, *6*, 216.

[35] N. Ortiz-Vitoriano, T. P. Batcho, D. G. Kwabi, B. Han, N. Pour, K. P. C. Yao, C. V. Thompson, Y. Shao-Horn, *J. Phys. Chem. Lett.* **2015**, *6*, 2636.
[36] J. E. Nichols, B. D. McCloskey, *J. Phys. Chem. C* **2017**, *121*, 85.
[37] P. Zhang, L. Liu, X. He, X. Liu, H. Wang, J. He, Y. Zhao, *J. Am. Chem. Soc.* **2019**, *141*, 6263.
[38] J. M. Tarascon, M. Armand, *Nature* **2001**, *414*, 359.
[39] M. Stich, M. Göttlinger, M. Kurniawan, U. Schmidt, A. Bund, *J. Phys. Chem. C* **2018**, *122*, 8836.
[40] A. Guéguen, D. Streich, M. He, M. Mendez, F. F. Chesneau, P. Novák, E. J. Berg, *J. Electrochem. Soc.* **2016**, *163*, A1095.
[41] Q. Sun, H. Yadegari, M. N. Banis, J. Liu, B. Xiao, X. Li, C. Langford, R. Li, X. Sun, *J. Phys. Chem. C* **2015**, *119*, 13433.
[42] A. Laforgue, M. Toupin, A. Mokrini, M. Gauthier, C. Bock, M. Ionescu, B. Luan, X. Z. Yuan, W. Qu, J. Y. Huot, *World Electr. Veh. J.* **2016**, *8*, 398.
[43] M. L. Pegis, B. A. McKeown, N. Kumar, K. Lang, D. J. Wasylenko, X. P. Zhang, S. Raugei, J. M. Mayer, *ACS Cent. Sci.* **2016**, *2*, 850.
[44] B. Lee, Y. Ko, G. Kwon, S. Lee, K. Ku, J. Kim, K. Kang, *Joule* **2018**, *2*, 61.
[45] G. A. Jeffrey, H. Maluszynska, J. Mitra, *Int. J. Biol. Macromol.* **1985**, *7*, 336.
[46] V. Marcano, P. Benitez, J. Campins, P. Matheus, C. Cedeño, N. Falcon, E. Palacios-Prü, *Planet. Space Sci.* **2004**, *52*, 613.
[47] F. W. Wilburn, *Thermochim. Acta* **1989**, *149*, 395.
[48] Y. Tanaka, T. Nakamura, *Nippon Kagaru Kaishi* **1975**, *1975*, 705.
[49] S. Wang, B. Ru, H. Lin, Z. Luo, *Bioresour. Technol.* **2013**, *143*, 378.
[50] Y. H. Roos, F. Franks, M. Karel, T. P. Labuza, H. Levine, M. Mathlouthi, D. Reid, E. Shalaev, L. Slade, *J. Agric. Food Chem.* **2012**, *60*, 10359.
[51] S. Wang, Y. Zhang, J. Zhang, S. Wang, Z. Tan, Q. Shi, *J. Therm. Anal. Calorim.* **2018**, *133*, 1049.
[52] J. H. F. de Jesus, A. P. G. Ferreira, E. T. G. Cavalheiro, *Food Chem.* **2018**, *258*, 199.
[53] F. Suárez-García, A. Martínez-Alonso, J. M. D. Tascón, *Carbon* **2004**, *42*, 1419.
[54] T. Stolar, S. Lukin, J. Požar, M. Rubčić, G. M. Day, I. Biljan, D. Š. Jung, G. Horvat, K. Užarević, E. Meštrović, I. Halasz, *Cryst. Growth Des.* **2016**, *16*, 3262.
[55] M. A. Posthumus, N. M. M. Nibbering, A. J. H. Boerboom, H. R. Schulten, *Biol. Mass Spectrom.* **1974**, *1*, 352.
[56] A. M. Naglah, M. A. Al-Omar, M. A. Bhat, A. S. Al-Wasidi, A. M. A. Alsuhaibani, A. M. El-Didamony, N. Hassan, S. A. Taleb, M. S. Refat, *Crystals* **2019**, *9*, 208.
[57] L. S. Shlyakhtenko, A. A. Gall, J. J. Weimer, D. D. Hawn, Y. L. Lyubchenko, *Biophys. J.* **1999**, *77*, 568.
[58] H. Zhang, T. Kuila, N. H. Kim, D. S. Yu, J. H. Lee, *Carbon* **2014**, *69*, 66.
[59] M. Enterría, J. L. Figueiredo, *Carbon* **2016**, *108*, 79.
[60] W. Luo, X. Zhao, W. Cheng, Y. Zhang, Y. Wang, G. Fan, *Nanoscale Adv.* **2020**, *2*, 1685.
[61] A. M. Puziy, O. I. Poddubnaya, R. P. Socha, J. Gurgul, M. Wisniewski, *Carbon* **2008**, *46*, 2113.
[62] B. J. Aylett, *Polyhedron* **1985**, *4*, 1799.
[63] R. Ma, G. Lin, Y. Zhou, Q. Liu, T. Zhang, G. Shan, M. Yang, J. Wang, *npj Comput. Mater.* **2019**, *5*, 78.
[64] I. M. Rocha, O. S. G. P. Soares, D. M. Fernandes, C. Freire, J. L. Figueiredo, M. F. R. Pereira, *ChemistrySelect* **2016**, *1*, 2522.
[65] G. Murdachaew, K. Laasonen, *J. Phys. Chem. C* **2018**, *122*, 25882.
[66] G. Wu, A. Santandreu, W. Kellogg, S. Gupta, O. Ogoke, H. Zhang, H. L. Wang, L. Dai, *Nano Energy* **2016**, *29*, 83.
[67] Y. Zhao, R. Nakamura, K. Kamiya, S. Nakanishi, K. Hashimoto, *Nat. Commun.* **2013**, *4*, 1.
[68] H. Deng, Q. Li, J. Liu, F. Wang, *Carbon* **2017**, *112*, 219.
[69] A. Farzaneh, N. Saghatoleslami, E. K. Goharshadi, H. Gharibi, H. Ahmadzadeh, *Electrochim. Acta* **2016**, *222*, 608.
[70] G. Wu, N. H. MacK, W. Gao, S. Ma, R. Zhong, J. Han, J. K. Baldwin, P. Zelenay, *ACS Nano* **2012**, *6*, 9764.
[71] Y. J. Wang, Y. Rusheng, A. Ignaszak, D. P. Wilkinson, Z. Jiujun, *Advanced Bifunctional Electrochemical Catalysts for Metal-Air Batteries*, CRC Press, Boca Raton **2019**.
[72] A. Kormányos, M. S. Hossain, F. W. Foss, C. Janáky, K. Rajeshwar, *Catal. Sci. Technol.* **2016**, *6*, 8441.
[73] R. Shibuya, T. Kondo, J. Nakamura, *ChemCatChem* **2018**, *10*, 2019.
[74] Y. Xu, C. Chen, M. Zhou, G. Fu, Y. Zhao, Y. Chen, *RSC Adv.* **2017**, *7*, 26722.